HTML ABSTRACT • LINKS

JOURNAL OF APPLIED PHYSICS VOLUME 95, NUMBER 1 1 JANUARY 2004

Growth, surface morphology, and electrical resistivity of fully strained substoichiometric epitaxial TiN_x ($0.67 \leqslant x < 1.0$) layers on MgO(001)

C.-S. Shin
Frederick Seitz Materials Research Laboratory and the Materials Science Department, University of Illinois, 104 South Goodwin, Urbana, Illinois 61801 and System IC R&D Center, Hynix Semiconductor, Inc., Cheongju, Korea

S. Rudenja, D. Gall, N. Hellgren, T.-Y. Lee, I. Petrov,[a] and J. E. Greene
Frederick Seitz Materials Research Laboratory and the Materials Science Department, University of Illinois, 104 South Goodwin, Urbana, Illinois 61801

(Received 7 August 2003; accepted 2 October 2003)

We have grown single-crystal NaCl-structure δ-TiN_x layers with x ranging from 0.67 to 1.00 on MgO(001) at 700 °C by ultra-high-vacuum reactive magnetron sputtering of Ti in mixed Ar/N_2 discharges in order to investigate microstructural evolution and the physical properties of TiN_x as a function of the N vacancy concentration. High-resolution x-ray diffraction and transmission electron microscopy results show that all layers grow with a cube-on-cube epitaxial relationship to the substrate, $(001)_{TiN}\|(001)_{MgO}$ and $[100]_{TiN}\|[100]_{MgO}$. The relaxed lattice parameter $a_o(x)$ decreases linearly from 4.240 Å with $x=1.00$ to 4.226 Å with $x=0.67$. Stoichiometric TiN(001) layers are fully relaxed at the growth temperature while layers with $0.67 \leqslant x \leqslant 0.92$ are fully coherent with their substrates. Surface morphologies vary dramatically with x. $TiN_x(001)$ layers with $x=0.67-0.82$ have very flat surfaces arising from large cation surface diffusion lengths approaching values corresponding to step flow. However, the surfaces of the $TiN_{0.92}(001)$ and $TiN_{1.00}(001)$ layers, which were grown at higher N_2 partial pressures, consist of a periodic two-domain ripple structure along the $\langle 110 \rangle$ directions due to kinetic roughening associated with lower cation surface mobilities resulting from higher steady state N coverages. $TiN_{1.0}(001)$ layers grown in pure N_2 exhibit growth mounds that are predominantly square with edges aligned along the $\langle 110 \rangle$ directions. The room-temperature resistivity, 13 $\mu\Omega$ cm with $x=1.00$, increases from 52 $\mu\Omega$ cm for $TiN_x(001)$ layers with $x=0.92$ to 192 $\mu\Omega$ cm with $x=0.67$, due primarily to increased carrier scattering from N vacancies. © *2004 American Institute of Physics.* [DOI: 10.1063/1.1629155]

I. INTRODUCTION

Transition-metal (TM) nitrides are well known for their remarkable physical properties including high hardness and mechanical strength, chemical inertness, high temperature stability, and low resistivity. As a result, they have become technologically important for applications such as hard wear-resistant coatings, diffusion barriers, and optical coatings. NaCl-structure δ-TiN has received by far the most attention and is now used commercially in all of the above applications. The layers are typically deposited by reactive magnetron sputtering and are generally understoichiometric as the N_2 partial pressure during reactive film growth is minimized in order to achieve deposition rates close to those of pure metal films.

NaCl-structure δ-TiN_x has a wide single-phase field extending from $x \simeq 0.6$ to 1.2.[1] Deviation from stoichiometry has been attributed to anion vacancies for $x<1$ and interstitial N atoms for $x>1$.[2] Stoichiometric single-crystal TiN layers with all three low-index orientations have been grown[3] and their physical properties measured.[3–5] Single-crystal TiN(001), for example, is metallic with a room-temperature resistivity $\rho = 13$ $\mu\Omega$ cm,[4,5] a hardness H of $\simeq 21$ GPa,[3] and a distinctive gold color due to intraband transitions giving rise to a high reflectance in the red and infrared.[6] Activation energies for adatom transport on atomically flat TiN(001) and TiN(111) surfaces have been determined from analyses of two-dimensional island coarsening measurements using *in situ* scanning tunneling microscopy.[7,8]

In contrast, little is known about the fundamental properties of substoichiometric TiN_x layers in spite of their commercial importance. Reported values for TiN_x properties can vary over orders of magnitude due primarily to large differences in stoichiometry, microstructure, and purity with, in most cases, the films being poorly characterized. For example, published resistivities range from 25 to 4500 $\mu\Omega$ cm.[9–11] For the few cases in which film stoichiometry was measured, ρ values were found to increase with decreasing x from 25–60 $\mu\Omega$ cm with $x=1$ to 80–100 $\mu\Omega$ cm with $x \simeq 0.7$.[10,11]

In order to provide a basis for comparing and interpreting measured properties of polycrystalline TiN_x, we report on the growth, surface morphology, and physical properties of well-characterized single-crystal substoichiometric ($x=0.67-0.92$) and stoichiometric $TiN_x(001)$ layers. The films were grown on MgO(001) at 700 °C by ultra-high-vacuum (UHV) reactive magnetron sputter deposition in mixed Ar/N_2 atmospheres as a function of the N_2 fraction

[a]Electronic mail: petrov@uiuc.edu

Downloaded 24 Feb 2004 to 130.126.102.130. Redistribution subject to AIP license or copyright, see http://jap.aip.org/jap/copyright.jsp

f_{N_2} at a constant total pressure of 20 mTorr. x ranged from 0.67 with $f_{N_2}=0.028$ to 0.92 with $f_{N_2}=0.035$. Stoichiometric TiN(001) layers were obtained with f_{N_2} spanning the entire range from 0.040 to 1.000. Relaxed lattice parameters a_o, determined from high-resolution (HR) reciprocal lattice maps (RLMs), increase linearly with increasing x from 4.226 Å with $x=0.67$ to 4.240 Å with $x=1$. All substoichiometric $TiN_x(001)$ layers are fully strained and commensurate with their substrates while stoichiometric TiN(001) layers are fully relaxed at the growth temperature. $TiN_x(001)$ surface morphologies evolve from predominantly flat to surfaces with ripple structures elongated along $\langle 110 \rangle$ directions to square growth mounds with edges aligned along $\langle 110 \rangle$ directions with increasing x. ρ increases from 52 $\mu\Omega$ cm with $x=0.92$ to 192 $\mu\Omega$ cm with $x=0.67$ due to increased carrier scattering by anion vacancies.

II. EXPERIMENTAL PROCEDURE

All $TiN_x(001)$ layers were grown to a thickness of 0.26 μm in a load-locked UHV magnetically unbalanced stainless-steel dc magnetron sputter deposition system described in detail in Refs. 12 and 13. The pressure in the sample introduction chamber was reduced to less than 5×10^{-8} Torr (7×10^{-6} Pa), using a $50\ \mathrm{l\,s^{-1}}$ turbomolecular pump (TMP), prior to initiating substrate exchange into the deposition chamber, which has a base pressure of 5×10^{-10} Torr (7×10^{-8} Pa), achieved using a $500\ \mathrm{l\,s^{-1}}$ TMP. A water-cooled 7.6-cm-diam Ti target with a purity of 99.997% was mounted 6 cm from the substrate holder. Sputter deposition was carried out at a constant current of 0.55 A and a total pressure of 20 mTorr (2.67 Pa) in mixed Ar (99.999% pure) and N_2 (99.999%) atmospheres for which the N_2 fraction f_{N_2} was varied, in separate experiments, from 0 to 1. During deposition, the pressure was monitored by a capacitance manometer and maintained constant with automatic mass-flow controllers.

A pair of external Helmholtz coils with Fe pole pieces were utilized to create a uniform axial magnetic field $B_{ext}=60$ G in the region between the target and the substrate. B_{ext} has a strong influence on the ion flux incident at the substrate, with only a minor effect on the target atom flux, and provides, as determined by electrostatic probe measurements,[12] an independently adjustable ion-to-metal flux ratio J_i/J_{Ti}. In the present film growth experiments, the incident ion energy E_i remained constant at 20 ± 2 eV over the full f_{N_2} range while J_i/J_{Ti} increased continuously from 0.8 with $f_{N_2}=0.025$ to 4.0 with $f_{N_2}=1$ due primarily to a decreasing film growth rate $R(f_{N_2})$.

The substrates were polished $10\times10\times0.5\ \mathrm{mm}^3$ MgO(001) wafers, cleaned with successive rinses in ultrasonic baths of trichloroethane, acetone, methanol, and deionized water and blown dry with dry N_2. The wafers were then mounted on resistively heated Ta platens using Mo clips and inserted into the sample introduction chamber for transport to the growth chamber where they were thermally degassed at 800 °C for 1 h, a procedure shown to result in sharp MgO(001)1×1 reflection high-energy electron diffraction patterns.[14] Immediately prior to initiating deposition, the target was sputter etched for 5 min with a shutter shielding the substrate. All TiN layers were grown at $T_s=700$ °C, including the contribution due to plasma heating. T_s was measured with a pyrometer calibrated by a thermocouple bonded to a dummy TiN-coated MgO substrate. Following deposition, the samples were allowed to cool below 100 °C before transferring them to the load-lock chamber, which was then vented with dry N_2.

The compositions and microstructures of as-deposited samples were determined using a combination of Rutherford backscattering spectrometry (RBS), x-ray diffraction (XRD), and atomic force microscopy (AFM) analyses. The RBS probe beam consisted of 2 MeV He^+ ions incident at an angle of 22.5° relative to the sample surface normal with the detector set at a 150° scattering angle. The total accumulated ion dose was 100 μC. Backscattered spectra were analyzed using the RUMP simulation program,[15] and the uncertainty in reported N/Ti ratios is less than ±0.03.

A high-resolution Philips X-pert MRD diffractometer with a Cu $K\alpha_1$ source ($\lambda=1.540\,597$ Å) and a four-crystal Ge(220) monochromator was used for the XRD measurements. A two-crystal Ge(220) analyzer was placed in front of the detector to provide an angular divergence of <12 arc s with a wavelength spread $\Delta\lambda/\lambda\simeq7\times10^{-5}$. Lattice parameters $a_\perp$ along the growth direction, in-plane lattice parameter $a_\parallel$, and residual strains ε were obtained from HR RLMs around asymmetric 113 reflections. The maps were obtained from a series of ω–2θ scans at different ω offsets.

Surface morphologies and roughnesses were quantified by AFM using a Digital Instruments Nanoscope II instrument operated in the contact mode. Several $3\times3\ \mu\mathrm{m}^2$ areas were scanned on each sample using oxide-sharpened Si_3N_4 tips with radii of 5–40 nm. Four-point-probe measurements were used to determine room-temperature resistivities ρ.

III. RESULTS AND DISCUSSION

A. Reactive sputter deposition

Initial experiments were carried out to characterize the kinetics of TiN_x reactive sputter deposition as a function of the N_2 fraction f_{N_2}. Figure 1 shows the effects of f_{N_2} on the target voltage V_T, film growth rate R, and resulting layer composition $x=$N/Ti. Both V_T and x initially increase very rapidly, while R decreases, with increasing f_{N_2}. Further changes, with $f_{N_2}\gtrsim0.04$, are less dramatic. The combined results in Fig. 1 can be understood based upon previous models for reactive sputtering.[16,17]

At low f_{N_2} values, all N_2 added to the discharge is consumed by Ti atoms being deposited at the substrate, as well as throughout the deposition chamber, in a heterogeneous surface-catalyzed reaction to form TiN_x. The film composition x varies approximately linearly from $x=0.53$ with $f_{N_2}=0.025$ to $x=1.00$ with $f_{N_2}\simeq0.04$, thereafter remaining constant at $x=1$ as f_{N_2} is increased further to 1.0. Raising f_{N_2} also results in the Ti target surface becoming increasingly nitrided. Since the secondary electron yield of TiN is less than that of Ti,[16] V_T floats up from 260 V with f_{N_2}

Downloaded 24 Feb 2004 to 130.126.102.130. Redistribution subject to AIP license or copyright, see http://jap.aip.org/jap/copyright.jsp

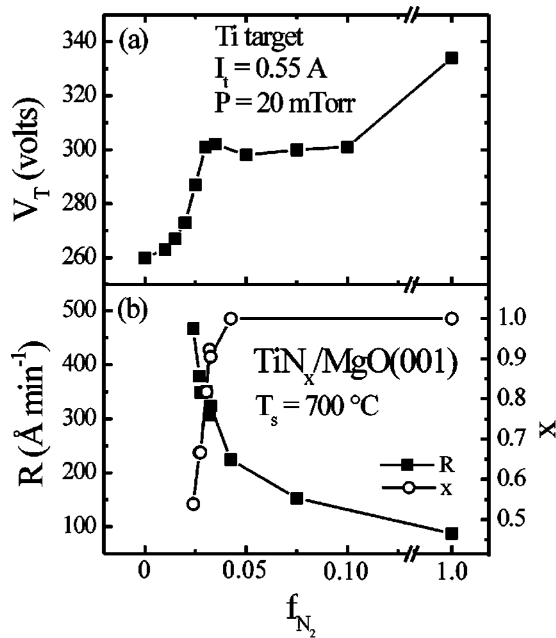

FIG. 1. (a) Target voltage V_T during reactive magnetron sputter deposition of epitaxial TiN_x layers grown on MgO(001) at $T_s = 700$ °C in mixed N_2/Ar atmospheres as a function of the N_2 fraction f_{N_2}. (b) Film growth rate R and N/Ti ratio x vs f_{N_2}.

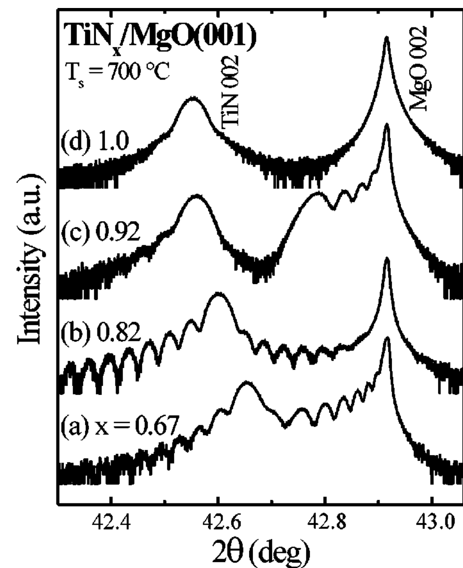

FIG. 2. HR-XRD ω–2θ scans from epitaxial δ-TiN_x layers grown on MgO(001) by ultra-high-vacuum reactive magnetron sputter deposition at $T_s = 700$ °C in mixed N_2/Ar atmospheres with N_2 fractions f_{N_2}. (a) $x = 0.67$ ($f_{N_2} = 0.028$), (b) $x = 0.82$ ($f_{N_2} = 0.030$), (c) $x = 0.92$ ($f_{N_2} = 0.032$), and (d) $x = 1.00$ ($f_{N_2} = 1.000$).

$= 0$ to 302 V with $f_{N_2} = 0.035$ in order to maintain the discharge current constant. Even with the increase in target voltage, the TiN_x deposition rate R exhibits a precipitous drop from 467 Å min^{-1} with $f_{N_2} = 0.025$ to 224 Å min^{-1} with $f_{N_2} = 0.043$ as the target surface becomes fully nitrided. This is primarily due to the lower sputtering yield of TiN compared to Ti.[13]

The relatively slow increase in V_T with $f_{N_2} \gtrsim 0.04$ [Fig. 1(a)] is due primarily to plasma volume ionization processes gradually shifting from being Ar dominated to N_2 dominated. The ionization efficiency decreases as a result of the increasing thermalization of discharge electrons arising from the large cross section for inelastic collisions which excite vibrational modes in N_2 molecules.[18] R continues to decrease, but much more slowly, as $f_{N_2} \rightarrow 1$ due to the lower sputtering yield of N_2^+ ions resulting from the poorer mass match between N_2 and Ti, compared to Ar and Ti, together with the lower secondary-electron yield and plasma volume ionization efficiency as discussed above.

B. Microstructure, surface morphology, and physical properties of $TiN_x(001)$ layers

Single-crystal B1 NaCl-structure δ-$TiN_x(001)$ layers with $x = 0.67$–1.00 were grown on MgO(001) at 700 °C using f_{N_2} values between 0.028 and 1.0. Decreasing f_{N_2} even slightly to 0.025 results in films that are two-phase and polycrystalline consisting of tetragonal ε-Ti_2N and δ-TiN grains with an overall film composition of $TiN_{0.53}$.

Figure 2 shows typical HR XRD ω–2θ scans from $TiN_x(001)$ layers with $x = 0.67$, 0.82, 0.92, and 1.00 grown with $f_{N_2} = 0.028$, 0.030, 0.032, and 1.000, respectively. 002 TiN and MgO peaks are the only observable features over the 2θ range 20°–80°. The peak centered at 42.916° ($a_{MgO} = 4.2112$ Å) is the MgO 002. The TiN_x 002 peak position ranges from 42.654° with $x = 0.67$ ($f_{N_2} = 0.028$) to 42.560° with $x = 0.92$ ($f_{N_2} = 0.032$) due to changes in film composition and residual strain. For layers with $x = 1$ ($0.043 \leqslant f_{N_2} \leqslant 1.000$), the TiN 002 peak occurs at $2\theta = 42.552$°, yielding an out-of-plane lattice parameter $a_\perp$ along the film growth direction of 4.2457 Å. For all single-phase $TiN_x(001)$ layers, XRD scans obtained in the parallel-beam mode about the azimuthal angle ϕ with ω and 2θ angles optimized for the 220 peaks of MgO and TiN at a tilt angle of 45° with respect to the surface normal, exhibit four 90°-rotated 220 peaks at the same ϕ angles for both MgO and TiN (see, for example, Fig. 3). The combined results show that the layers are single crystal with a cube-on-cube epitaxial relationship to the substrate, $(001)_{TiN} \| (001)_{MgO}$ and $[100]_{TiN} \| [100]_{MgO}$.

Finite-thickness interference fringes, clearly visible in HR XRD scans from all substoichiometric $TiN_x(001)$ layers,

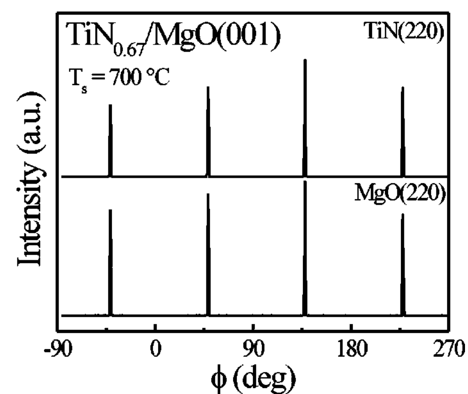

FIG. 3. XRD 220 ϕ scans from an epitaxial δ-$TiN_{0.67}$ layer grown on MgO(001) at $T_s = 700$ °C with $f_{N_2} = 0.028$.

Downloaded 24 Feb 2004 to 130.126.102.130. Redistribution subject to AIP license or copyright, see http://jap.aip.org/jap/copyright.jsp

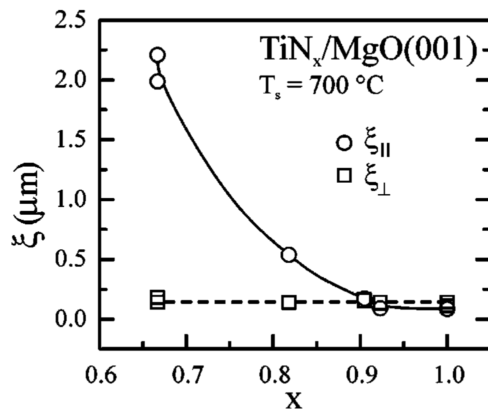

FIG. 4. In-plane $\xi_\parallel$ and perpendicular $\xi_\perp$ x-ray coherence lengths in epitaxial TiN_x layers grown on MgO(001) at $T_s = 700$ °C as a function of x.

indicate that the films are of high structural quality with a laterally uniform substrate/film interface. We attribute the higher crystalline quality of the substoichiometric layers, compared to the stoichiometric TiN(001) layers for which no interference fringes are obtained, to increased cation surface mobilities during growth under N deficient conditions corresponding to lower N steady-state coverages. From the fringe spacings, we obtain layer thicknesses of 2630 Å for the $x = 0.67$ layer [Fig. 2(a)] and 2590 Å for the $x = 0.82$ layer [Fig. 2(b)], in good agreement with values from the deposition rate calibrations.

In-plane and orthogonal x-ray coherence lengths $\xi_\parallel$ and $\xi_\perp$ were determined from the widths of the 002 diffracted intensity distributions perpendicular $\Delta g_\perp$ and parallel $\Delta g_\parallel$, respectively, to the diffraction vector $\bar{g}$ using the relationships[19]

$$\xi_\parallel = 2\pi/|\Delta g_\perp| = \lambda/[2\Gamma_\omega \sin\theta], \quad (1)$$

and

$$\xi_\perp = 2\pi/|\Delta g_\parallel| = \lambda/[\Gamma_{2\theta} \cos\theta]. \quad (2)$$

Γ_ω and $\Gamma_{2\theta}$ are the full width at half maximum intensities of the 002 Bragg peak in the ω and 2θ directions. Figure 4 shows that $\xi_\parallel$, a measure of the lateral (in-plane) film crystalline quality, decreases from 2.2 μm for layers with $x = 0.67$ to 0.54μm with $x = 0.82$ to 0.09 μm with $x = 0.92$. $\xi_\parallel(x)$ then remains approximately constant with further increases in x to 1.00. ($\xi_\parallel$ is also constant as a function of f_{N_2} for all $x = 1$ layers). In contrast, $\xi_\perp$ values, determined by finite thickness effects as well as vertical (out-of-plane) crystalline quality, do not change appreciably as a function of x with values ranging from 0.13 to 0.19 μm, which is a significant fraction of the thickness of these layers, $\simeq 0.26$ μm. Thus, $TiN_{0.67}(001)$ films exhibit the lowest mosaicity and highest crystalline quality. Comparing $\xi_\parallel$ values to reported results for other epitaxial transition-metal nitrides [150 Å for ScN(001),[20] 210 Å for δ-TaN(001),[21] and 800 Å for CrN(001)[22], the x-ray coherence lengths for substoichiometric $TiN_{0.67}(001)$ layers are approximately 30–150× larger. We ascribe this, as discussed below, to both a lower film/substrate lattice mismatch and higher cation surface mobilities resulting from lower steady-state N coverages during growth of substoichiometric $TiN_x(001)$ layers.

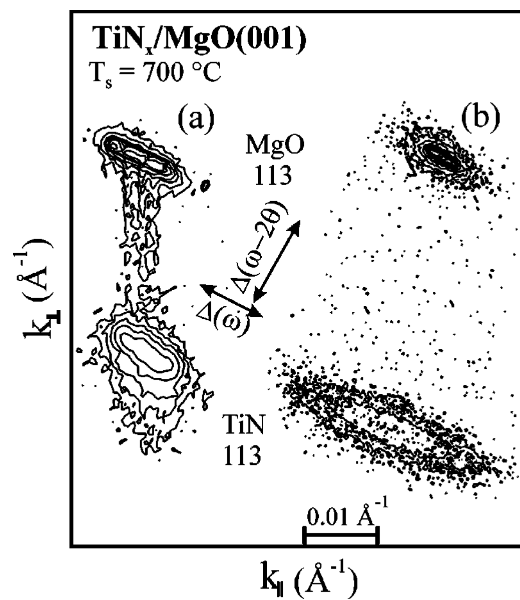

FIG. 5. HR RLMs around the 113 reflection of epitaxial TiN_x layers grown on MgO(001) at $T_s = 700$ °C. (a) $x = 0.67$ and (b) $x = 1.00$.

In-plane $a_\parallel$, out-of-plane $a_\perp$, and relaxed a_o lattice parameters of epitaxial $TiN_x(001)$ layers were determined as a function of x from HR-RLM results. Typical HR RLMs about the asymmetric 113 reflection are shown in Fig. 5 for layers with $x = 0.67$ and 1.00. Diffracted intensity distributions are plotted as isointensity contours as a function of the reciprocal lattice vectors $k_\parallel$ parallel and $k_\perp$ perpendicular to the surface.[23] For the 113 reflection from a 001-oriented NaCl-structure sample, the in-plane and out-of-plane lattice parameters are given by $a_\parallel = \sqrt{2}/k_\parallel$ and $a_\perp = 3/k_\perp$. Lattice parameter values obtained from the HR RLMs in Fig. 5 are $a_\parallel = 4.2099$ Å and $a_\perp = 4.2345$ Å for the $x = 0.67$ layer with $a_\parallel = 4.2289$ Å and $a_\perp = 4.2458$ Å for the $x = 1.00$ layer.

The fact that the substrate and layer peaks for the $x = 0.67$ sample [Fig. 5(a)] are aligned along $k_\parallel$ to within the instrument detection limit, $\simeq 2\times10^{-5}$, indicates that the film is fully strained. Corresponding measurements for the other samples show that all substoichiometric ($x \leqslant 0.92$) $TiN_x(001)$ layers are also fully coherent with their MgO(001) substrates. In contrast, substrate and layer peaks in the $x = 1.00$ HR RLM [Fig. 5(b)] are misaligned along $k_\parallel$, revealing the presence of in-plane-strain relaxation due to misfit dislocations. The residual strain, $\varepsilon_\parallel = -0.26\%$, of stoichiometric layers can be fully accounted for by differential thermal contraction during sample cooling following deposition at 700 °C. The thermal expansion coefficients of TiN and MgO are 9.35×10^{-6} K^{-1} (Ref. 24) and 1.3×10^{-5} K^{-1},[25] resulting in a thermal strain of -0.27%, which is identical, within experimental uncertainty, to the measured strain. Therefore, stoichiometric layers are fully relaxed at the growth temperature.

There is a dramatic difference between substoichiometric layers that are fully strained with no detectable misfit dislocations and stoichiometric layers that are fully relaxed

Downloaded 24 Feb 2004 to 130.126.102.130. Redistribution subject to AIP license or copyright, see http://jap.aip.org/jap/copyright.jsp

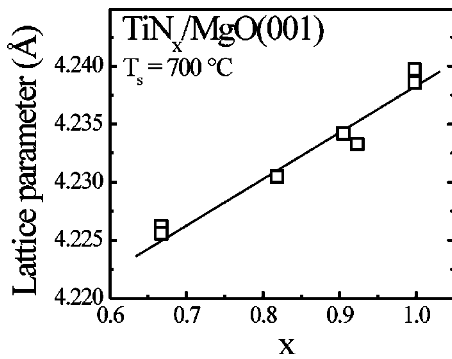

FIG. 6. Relaxed lattice parameters a_o of epitaxial TiN_x layers grown on MgO(001) at $T_s = 700\,°C$ as a function of x.

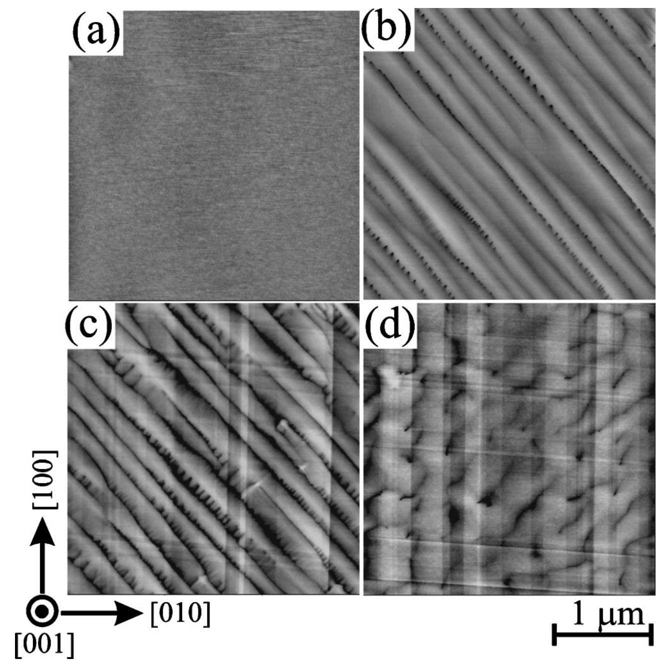

FIG. 7. Atomic force microscopy images ($3 \times 3\ \mu m^2$) from epitaxial TiN_x layers grown on MgO(001) at $T_s = 700\,°C$ with (a) $x = 0.82$ ($f_{N_2} = 0.030$), (b) $x = 0.92$ ($f_{N_2} = 0.032$), (c) $x = 1.00$ ($f_{N_2} = 0.043$), and (d) $x = 1.00$ ($f_{N_2} = 1.000$).

at the growth temperature. This can be, at least, partially ascribed to the compositional dependence of the film/substrate lattice mismatch $m(x) = [a_o(x) - a_{MgO}]/a_{MgO}$ at $T_s = 700\,°C$. m is 0.43% at $x = 1.00$, but decreases with increasing N vacancy concentration to 0.10% at $x = 0.67$, thus reducing the driving force for the nucleation of misfit dislocations.

Relaxed bulk $TiN_x(001)$ lattice parameters a_o were determined from $a_\parallel$ and $a_\perp$ values through the relationship

$$a_o = a_\perp \left(1 - \frac{2\nu(a_\perp - a_\parallel)}{a_\perp(1+\nu)} \right), \tag{3}$$

where $\nu = 0.22$ is the TiN Poisson ratio.[26] As shown in Fig. 6, $a_o(x)$ decreases approximately linearly from 4.2397 Å with $x = 1.00$ to 4.2333 Å with $x = 0.92$, reaching 4.2256 Å at $x = 0.67$. Our $a_o(x)$ results for understoichiometric $TiN_x(001)$ layers are in good agreement with published values for bulk polycrystalline TiN_x samples,[2] as well as reported results from N-implanted epitaxial Ti layers.[27]

We attribute the observed decrease in a_o at lower $TiN_x(001)$ x values to a corresponding increase in the N vacancy concentration. From the results in Fig. 6, the rate of change in the normalized $TiN_x(001)$ lattice constant as a function of x, $\zeta = d[a_o(x)/a_{o,TiN}]/dx$, where $a_{o,TiN}$ is the relaxed lattice constant of stoichiometric TiN, is small. $\zeta = +0.040$, in agreement with values obtained from measurements of the density of bulk TiN_x samples with $x = 0.5 - 1.0$.[2]

AFM investigations reveal striking changes in $TiN_x(001)$ surface morphologies as a function of x. Figure 7 shows typical $3 \times 3\ \mu m^2$ AFM images from $TiN_x(001)$ layers grown at $T_s = 700\,°C$ with $x = 0.82$ ($f_{N_2} = 0.030$), 0.92 ($f_{N_2} = 0.032$), 1.0 ($f_{N_2} = 0.043$), and 1.0 ($f_{N_2} = 1.000$). The surface morphologies of the $TiN_{0.67}$ and $TiN_{0.82}(001)$ [Fig. 7(a)] layers are essentially identical. Both are atomically smooth with surface widths w, equivalent to the root-mean-square (rms) roughness, of 1.5 Å. This is less than the TiN(001) monoatomic step height, 2.12 Å, and very close to the roughness of the MgO(001) substrate, $w = 1.3$ Å, for which an atomic-height step is 2.11 Å. w increases rapidly for layers grown with $f_{N_2} \geqslant 0.032$ ranging from 4.43 Å for $TiN_{0.92}(001)$ to 7.01 Å for TiN(001) ($f_{N_2} = 0.043$).

Figure 7 also shows that, in addition to w, the surface morphology changes with x. $TiN_{0.92}(001)$ and TiN(001) surfaces consist of ripple structures along the ⟨110⟩ directions with average periodicities of 0.17 and 0.22 μm, respectively, and an increasing tendency, at larger x values, for secondary dendritic structures to form along orthogonal ⟨110⟩ directions. Further increases in f_{N_2}, while they have no measurable effect on film stoichiometry, which remains constant at $x = 1$, continue to strongly affect the surface morphology. w decreases to 4.03 Å for TiN(001) layers grown in pure N_2 [Fig. 7(d)] and the surface exhibits growth mounds, which are predominantly square with edges aligned along the ⟨110⟩ directions. In addition to the growth mounds, surface slip steps produced by glide of misfit dislocations become apparent in $TiN_x(001)$ layers with $x = 1$, as shown in Figs. 7(c) and 7(d). This is fully consistent with our HR-RLM results presented above showing that layers with $x = 1$ are relaxed, i.e., contain misfit dislocations, while $TiN_x(001)$ films with $x = 0.67 - 0.92$ are completely coherent with their substrates due to a smaller lattice constant mismatch.

Ripple structures and growth mounds form due to kinetic surface roughening during deposition under conditions of low adatom mobility in the presence of Ehrlich barriers to adatom migration over descending step edges.[28] Their formation is exacerbated during sputter deposition due to the large component of non-normal deposition flux,[29] which results in atomic shadowing and, hence, a reduction in the fraction of flux reaching the valleys between mounds.

The very flat surfaces we obtain with $TiN_{0.67}(001)$ and $TiN_{0.82}(001)$ layers indicate that they grow under conditions approaching step flow with large cation surface diffusion lengths consistent with their large in-plane x-ray coherence length. Ti diffusion on $TiN_x(001)$ surfaces with low steady-

Downloaded 24 Feb 2004 to 130.126.102.130. Redistribution subject to AIP license or copyright, see http://jap.aip.org/jap/copyright.jsp

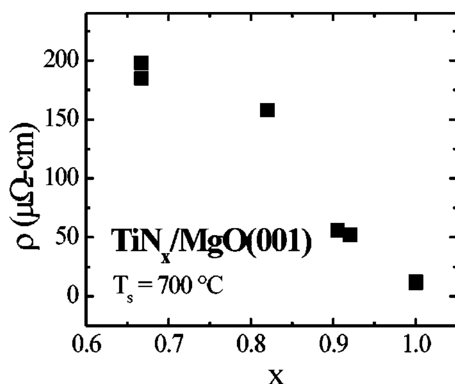

FIG. 8. Room-temperature resistivities ρ of epitaxial TiN_x layers grown on MgO(001) at $T_s = 700\,°C$ as a function of x.

state N coverages, which is the case for growth under N-deficient conditions, has a relatively low activation energy, calculated by *ab initio* density functional methods to be 0.37 eV.[30] Increasing f_{N_2} during deposition radically reduces the cation surface diffusion length due to the enhanced probability for encountering free N atoms and forming admolecules with much higher diffusion activation energies,[30] resulting in the surface kinetic roughening we observe for layers with $x \geq 0.92$.

The secondary dendritic structures which form along orthogonal ⟨110⟩ directions in $x \geq 0.82$ layers grown with increasing f_{N_2} are the result of a Bales–Zangwill instability.[31] That is, growth of the substoichiometric $TiN_x(001)$ layers proceeds under relatively high adatom mobility conditions, as noted earlier, in which adatom incorporation occurs primarily at step edges (rather then via island nucleation). This, in turn, results in denuded zones near ascending step edges with corresponding adatom concentration gradients extending out into the adjacent terraces. The surface steps themselves, which are rough on large length scales, are composed locally of low-energy 100 and 010 facets giving rise to alternating outward-facing convex corners and inward concave corners. The convex regions, due to the adatom concentration gradient, grow faster than the concave regions giving rise to the formation of dendritic or finger-like structures along perpendicular 110 directions.

Room-temperature resistivities ρ of $TiN_x(001)$ layers are plotted as a function of x in Fig. 8. ρ increases continuously from 13 $\mu\Omega$ cm with $x = 1.00$ to 190 $\mu\Omega$ cm with $x = 0.67$. The former value is in agreement with previously reported results for stoichiometric TiN(001).[4,5] As is the case for bulk TiC_x and TaC_x,[10,32] we attribute the overall increase in ρ with decreasing x to charge scattering by anion vacancies. $\rho(x)$ exhibits a steeper slope between $x = 0.8$ and 1.0 with a more gradual change for $x < 0.8$. This can be directly associated with changes in the TiN_x band structure, similar to reported results for $Ti_{1-x}Sc_xN(001)$ alloys.[4] The conduction electrons in stoichiometric TiN occupy three bands of which the upper two are degenerate and exhibit a higher curvature corresponding to a lower electron effective mass m^* (i.e., a higher electron mobility). As the N vacancy concentration increases in TiN_x, leading to a lowering of the Fermi level, the lower m^* bands are depopulated. This gives rise to a rapid decrease in the average electron mobility resulting in the observed steep slope in $\rho(x)$ at $x > 0.8$. In contrast, for $x < 0.8$, the change in $\rho(x)$ is relatively unaffected by the Fermi level position, as only a single low-mobility conduction band is populated. Consequently, $\rho(x)$ at $0.67 < x < 0.8$ is primarily determined by electron scattering, which leads to a weaker x dependence in ρ.

IV. CONCLUSIONS

Microstructure, surface morphology, relaxed lattice constants, x-ray coherence lengths, and the resistivity of NaCl-structure epitaxial understoichiometric $TiN_x(001)$ layers with controlled N concentrations have been determined as a function of x. The films were grown on MgO(001) at 700 °C by ultra-high-vacuum reactive sputtering of Ti in mixed Ar/N_2 discharges. Layers with N/Ti ratios x between 0.67 and 1.00 were obtained by varying the N_2 sputtering gas fraction f_{N_2} between 0.025 and 0.043. Further increases in f_{N_2} had no affect on layer composition, as the films remained stoichiometric, but strongly influenced film surface morphologies. Growth rates R initially decreased very rapidly with increasing f_{N_2} due to the corresponding increase in the steady-state N coverage on the Ti target combined with the lower sputtering yield of TiN than Ti. This was mediated slightly by the fact that TiN also has a lower secondary electron yield than Ti, which results in the target voltage floating up in order to maintain the discharge current constant. The target becomes fully poisoned (i.e., nitrided) at $f_{N_2} \simeq 0.04$. Further increases in f_{N_2} result in R continuing to decrease, but in a much slower manner, due primarily to plasma volume effects: the sputtering yield of N_2^+ ions is lower than that of Ar^+ and the addition of N_2, with its large cross section for inelastic collisions through the excitation of vibrational modes, tends to thermalize plasma electrons.

$TiN_x(001)$ layers with compositions spanning the entire equilibrium single-phase compound field were found to exhibit a cube-on-cube epitaxial relationship with the substrate, $(001)_{TiN} \| (001)_{MgO}$ and $[100]_{TiN} \| [100]_{MgO}$. Relaxed lattice parameters a_o decrease linearly from 4.2397 Å with $x = 1.00$ to 4.2256 Å with $x = 0.67$, thus reducing the mismatch with the substrate, due to the increased anion vacancy concentration. This, in turn, results in stoichiometric TiN(001) layers being fully relaxed at the growth temperature while layers with compositions $0.67 \leq x \leq 0.92$ are fully coherent with the substrate. Correspondingly, the room-temperature resistivity ρ of $TiN_x(001)$ increases approximately linearly from 13 $\mu\Omega$ cm for stoichiometric layers to 192 $\mu\Omega$ cm for $TiN_{0.67}(001)$, as a result of the increased carrier scattering associated with the N vacancies.

Surface morphologies of $TiN_x(001)$ layers vary dramatically as a function of f_{N_2} due to the resulting changes in the steady state N coverage θ_N at the surface of the growing film. Increases in θ_N decrease the cation surface diffusion length because of the enhanced probability for encountering free N atoms and forming admolecules with lower surface mobilities. This, gives rise to $TiN_x(001)$ surface morphologies which vary with increasing f_{N_2} from being extremely

Downloaded 24 Feb 2004 to 130.126.102.130. Redistribution subject to AIP license or copyright, see http://jap.aip.org/jap/copyright.jsp

flat ($f_{N_2} \leqslant 0.030$) with $w \leqslant 1.5$ Å to surfaces with rippled structures consisting of growth mounds elongated along ⟨110⟩-directions ($f_{N_2} = 0.032 - 0.043$) to growth mounds that are predominantly square with edges aligned along ⟨110⟩ directions in pure N_2.

ACKNOWLEDGMENTS

The authors gratefully acknowledge the financial support of the Department of Energy, Division of Materials Science, under Contract No. DEFG02-91ER45439 during the course of this research. The authors also appreciate the use of the facilities of the Center for Microanalysis of Materials, which is partially supported by DOE, at the University of Illinois. Two of the authors (S.R. and N.H.) are partially supported by the Fulbright Foundation and the Swedish Foundation for International Cooperation in Research and Higher Education (STINT), respectively.

[1] J.-E. Sundgren, B.-O. Johansson, A. Rockett, S. A. Barnett, and J. E. Greene, in *Physics and Chemistry of Protective Coatings*, edited by J. E. Greene, W. D. Sproul, and J. A. Thornton (American Institute of Physics, New York, 1986), Series 149, p. 95.
[2] L. E. Toth, *Transition Metal Carbides and Nitrides* (Academic, New York, 1971), p. 87, and references therein.
[3] H. Ljungcrantz, M. Odén, L. Hultman, J. E. Greene, and J.-E. Sundgren, J. Appl. Phys. **80**, 6725 (1996).
[4] D. Gall, I. Petrov, and J. E. Greene, J. Appl. Phys. **89**, 401 (2001).
[5] B. W. Karr, I. Petrov, P. Desjardins, D. G. Cahill, and J. E. Greene, Phys. Rev. B **61**, 16137 (2000).
[6] J.-E. Sundgren, B.-O. Johansson, and S.-E. Karlsson, Surf. Sci. **128**, 265 (1983).
[7] S. Kodambaka, V. Petrova, S. V. Khare, D. Gall, A. Rockett, I. Petrov, and J. E. Greene, Phys. Rev. Lett. **89**, 176102 (2002).
[8] S. Kodambaka, V. Petrova, A. Vailionis, I. Petrov, and J. E. Greene, Surf. Sci. **526**, 85 (2003).
[9] L. Y. Ting, J. Vac. Sci. Technol. **21**, 14 (1982).
[10] J.-E. Sundgren, B. O. Johansson, and S.-E. Karlsson, Thin Solid Films **105**, 353 (1983); J.-E. Sundgren, B. O. Johansson, and S.-E. Karlsson, and H. T. Henzell, *ibid.* **105**, 367 (1983).
[11] J. H. Kang and K. J. Kim, J. Appl. Phys. **86**, 346 (1999).
[12] F. Adibi, I. Petrov, L. Hultman, U. Wahlström, T. Shimazu, D. McIntyre, J. E. Greene, and J.-E. Sundgren, J. Appl. Phys. **69**, 6437 (1991).
[13] I. Petrov, F. Adibi, J. E. Greene, W. D. Sproul, and W.-D. Münz, J. Vac. Sci. Technol. A **10**, 3283 (1992).
[14] R. C. Powell, N.-E. Lee, Y.-W. Kim, and J. E. Greene, J. Appl. Phys. **73**, 189 (1998).
[15] R. L. Doolittle, Nucl. Instrum. Methods Phys. Res. B **15**, 344 (1985).
[16] I. Petrov, A. Myers, J. E. Greene, and J. R. Abelson, J. Vac. Sci. Technol. A **12**, 2846 (1994).
[17] I. Ivanov, L. Hultman, K. Järrendahl, P. Mårtensson, B. Hjörvarsson, and J. E. Greene, J. Appl. Phys. **78**, 5721 (1995).
[18] B. R. Natarajan, A. H. Eltoukhy, J. E. Greene, and T. L. Barr, Thin Solid Films **68**, 201 (1980).
[19] R. C. Powell, N.-E. Lee, Y.-W. Kim, and J. E. Greene, J. Appl. Phys. **73**, 189 (1998).
[20] D. Gall, I. Petrov, N. Hellgren, L. Hultman, J.-E. Sundgren, and J. E. Greene, J. Appl. Phys. **84**, 6034 (1998).
[21] C.-S. Shin, D. Gall, Y.-W. Kim, P. Desjardins, I. Petrov, and J. E. Greene, J. Appl. Phys. **90**, 2879 (2001).
[22] D. Gall, C.-S. Shin, T. Spila, M. Odén, M. J. H. Senna, J. E. Greene, and I. Petrov, J. Appl. Phys. **91**, 3589 (2002); D. Gall, C.-S. Shin, R. T. Haasch, I. Petrov, and J. E. Greene, *ibid.* **91**, 5882 (2002).
[23] P. van der Sluis, J. Phys. D **26**, A188 (1993).
[24] K. Aigner, W. Lengauer, D. Rafaja, and P. Ettmayer, J. Alloys Compd. **215**, 121 (1994).
[25] H. Landolt and R. Börnstein, *Numerical Data and Functional Relationships in Science and Technology, Group III* (Springer, Berlin, 1975), Vol. 7, Pt. b1, p. 27.
[26] J. A. Sue, Surf. Coat. Technol. **54/55**, 154 (1992).
[27] Y. Kasukabe, N. Saito, M. Suzuki, Y. Yamada, Y. Fujino, S. Nagata, M. Kishimoto, and S. Yamaguchi, J. Vac. Sci. Technol. A **16**, 3366 (1998).
[28] S. C. Wang and G. Ehrlich, Phys. Rev. Lett. **70**, 41 (1993); **71**, 4177 (1993); G. Ehrlich, Surf. Sci. **331/333**, 865 (1995); A. Gölzhäuser and G. Ehrlich, Phys. Rev. Lett. **77**, 1334 (1996).
[29] Sputter deposition, typically, results in a cosine distribution of the incoming atom flux with the highest flux at an azimuthal angle of 45°; H. Huang, G. H. Gilmer, and T. D. de la Rubia, J. Appl. Phys. **84**, 3636 (1998).
[30] D. Gall, S. Kodambaka, M. A. Wall, I. Petrov, and J. E. Greene, J. Appl. Phys. **93**, 9086 (2003).
[31] G. S. Bales and A. Zangwill, Phys. Rev. B **41**, 5500 (1989).
[32] L. E. Toth, *Transition Metal Carbides and Nitrides* (Academic, New York, 1971), p. 187 and references therein.

Downloaded 24 Feb 2004 to 130.126.102.130. Redistribution subject to AIP license or copyright, see http://jap.aip.org/jap/copyright.jsp